Morphology-Controlled WO_3 and WS_2 Nanocrystals for Improved Cycling Performance of Lithium Ion Batteries

Young Rok Lim[1], Yunseok Ko[1], Jeunghee Park[1]*, Won Il Cho[2], Soo A Lim[3]*, and EunHee Cha[3]*

[1]*Department of Chemistry, Korea University, Sejong 339-700, Korea*
[2]*Center for Energy convergence, Korea Institute of Science and Technology, Seoul 136-791, Korea*
[3]*Dept. of Pharmaceutical Engineering, Hoseo University, Asan, Chungnam 336-795, Korea*

ABSTRACT

As a promising candidate for anode materials in lithium ion battery (LIB), tungsten trioxide (WO_3) and tungsten disulfide (WS_2) nanocrystals were synthesized, and their electrochemical properties were comprehensibly studied using a half cell. One-dimensional WO_3 nanowires with uniform diameter of 10 nm were synthesized by hydrothermal method, and two-dimensional (2D) WS_2 nanosheets by unique gas phase sulfurization of WO_3 using H_2S. WS_2 nanosheets exhibits uniformly 10 nm thickness. The WO_3 nanowires and WS_2 nanosheets showed maximum capacities of 552 and 633 mA h g^{-1}, respectively, after 100 cycles. Especially, the capacity of WS_2 is significantly larger than the theoretical capacity (433 mA h g^{-1}). We also examined the cycling performance using a larger size WO_3 and WS_2 nanocrystals, showing that the smaller size plays an important role in enhancing the capacity of LIBs. The larger capacity of WS_2 nanosheets than the theoretical value is ascribed to the lower charge transfer resistance of 2D nanostructures.

Keywords : Tungsten oxide, Tungsten sulfide, Nanocrystals, Gas phase sulfurization, Lithium ion battery

1. Introduction

Rechargeable lithium ion batteries (LIBs) have become the dominant power sources for portable electronic devices, and their usage has now been expanded into larger units such as electric vehicles and robots, due to their high energy and power densities [1-4]. In recent years, transition metal oxide and sulfide compounds have been actively studied as the most promising alternative to commercial carbon anode materials for LIBs, because of their much higher theoretical capacity as compared with practical graphite (theoretical capacity: 372 mA h g^{-1}) [5-9]. When Li react with WO_3 to form three Li_2O, following the reaction of $WO_3 + 6Li^+ + 4e^- \rightarrow W + 3Li_2O$, the theoretical capacity of WO_3 is 693 mA h g^{-1}, which is close to twice that of graphite. A number of

works showed that WO_3 has a relatively high charge capacity, conductivity, and stability among various oxide materials [10-20].

Two-dimensional (2D) transition metal dichalcogenides (TMDs) have the similar structure as graphene, that is, a layered structure with a plane of metal atoms in between two planes of chalcogen atoms. WS_2, which is a representative material of TMDs, has strong covalent bonds in the S-W-S layer and weak van der Waals force between these layers, which can lead to efficient insertion and extraction of Li ions. The interlayer distance of WS_2 is 0.62 nm, which is wider than 0.335 nm of graphite, so it is predicted that diffusion and storage of Li ions will occur rapidly. It is predicted that WS_2 can be combined with four Li to form two Li_2S, following the reaction of $WS_2 + 4Li^+ + 4e^- \rightarrow W + 2Li_2S$, so that the theoretical capacity is 432 mA h g^{-1}, which is larger than graphite but less than WO_3. WS_2 alone often exhibit low cycling performance and fast capacity fading, caused by a large volume change during the charging/discharging cycle of LIBs like other cathode materials. Hence, they are usually used as com-

*E-mail address: parkjh@korea.ac.kr, limsooa@gmail.com, chaeunhee@hoseo.edu

posites with carbon nanomaterials (e.g., reduced graphene oxide, carbon nanotubes), resulting in enhanced cycling performance together with capacities even higher than the theoretical value [21-36].

In this study, we synthesized WO_3 and WS_2 nanostructures and measured their electrochemical performance of LIBs without any carbon supports. We used a simple hydrothermal method for high-yield synthesis of WO_3 nanowires that possess thin and long one-dimensional morphology. Remarkably, thin WS_2 nanosheets were synthesized by unique gas phase sulfurization of WO_3 using H_2S. Two kinds of WO_3 and WS_2 nanocrystals were synthesized; WO_3 nanocrystals and nanowires were named as WO-1 and WO-2, respectively, and WS_2 nanosheets made from them were named as WS-1 and WS-2, respectively. WO-1 has a particle shape with a mean diameter of 50 nm, while WO-2 has a nanowire shape with a 10 nm diameter uniformly. WS-1 synthesized using WO-1 is 5 times larger than WS-2 synthesized using WO-2. The results of this study will show that the use of morphology/size-controlled nanocrystals can significantly affect the charge-discharge capacity of LIBs, which will contribute to the development of high-performance LIB.

2. Experimental

Reagents. WO_3 nanopowder (tungsten trioxide, size: <50 nm) and WCl_6 (tungsten hexachloride, purity: 99.99 +%) were used in 99.9% of products from Sigma-Aldrich.

Synthesis. WO-1 was prepared from the purchased WO_3 nanopowder by removing volatile impurities under vacuum. WO-2 was synthesized by hydrothermal reaction as follows. Add 0.1 g of WCl_6 and 100 mL of EtOH into a beaker and stir for 60 minutes. The solution is placed in a Teflon container, placed in a stainless-steel reactor, cap tightly sealed, and subjected to hydrothermal reaction at 200°C for 24 hours. After the reaction was completed, the amorphous phase powders were collected. The product was washed with distilled water and dried under vacuum to evaporate the water. Then the product was placed in the furnace and annealed at 400°C under Ar gas flow, producing WO-2. For the synthesis of WS_2 nanocrystals, the WO_3 nanocrystals (WO-1 or WO-2) are placed in the center of the furnace and heated to 400°C under Ar gas flow. When the temperature

reaches 400°C, H_2S gas is flowed and reacted for 1 hour. The product (WS-1 and WS-2) was collected after the sulfurization.

Characterization. The products were characterized by scanning electron microscopy (SEM, Hitachi S-4700), field-emission transmission electron microscopy (FE TEM, FEI TECNAI G2 200 kV, Jeol JEM 2100F, HVEM), energy-dispersive X-ray fluorescence spectroscopy (EDX), and electron energy-loss spectroscopy (EELS, GATAN GIF-2000). Fast Fourier-transform (FFT) images were generated by the inversion of the TEM images using Digital Micrograph GMS1.4 software (Gatan Inc.). High-resolution X-ray diffraction (XRD) patterns were obtained using the 9B and 3D beamlines of the Pohang Light Source (PLS) with monochromatic radiation (l = 1.54595 Å). XRD pattern measurements were also carried out in a Rigaku D/MAX-2500 V/PC using Cu K_α radiation (λ = 1.54056 Å).

Electrochemical measurements of LIB half cells. The electrodes of the battery test cells were made of the active material, carbon black (Super P) and polyacrylic acid (PAA, 35 wt% dissolved in water; Aldrich) binder at a weight ratio of 6:2:2. In order to obtain the best performance, we adjusted the amount of the carbon black and found that 8:1:1 or 7:1:2, 6:2:2 was not much different. The distilled water-mixed slurry was coated onto the 10 mm-thick Cu foil. The coated electrode was dried at 80°C for 12 h and then roll-pressed. The thickness of the film was 150 μm. The active materials were loaded with 2 mg cm^{-2}. The coin-type half-cells (CR2032) were prepared in an argon-filled glove box. The LIB cell consisted of an electrode (containing the active material), the Li metal, a 25 mm microporous polyethylene separator (Celgard 2400), an electrolyte solution of 1 M $LiPF_6$ in 1:1:1 volume ratio of ethylene carbonate (EC), ethyl methyl carbonate, and dimethyl carbonate (DMC). Fluoroethylene carbonate (FEC) was used at 5 wt% as an electrolyte additive. Cyclic voltammetry (CV) measurements were conducted (Biology SAS) in a voltage range of 0.01-3 V at a rate of 0.1 mV s^{-1}. The performance of the cells was examined using a battery testing system (Maccor 4000) at a current density of 0.1-5 C between 0.01 and 3 V. We usually fabricated 3-5 LIB half-cells for each composition and took the data that represent the average value. In order to best performance, we adjusted the amount of the carbon black and found that 10-20 wt. % of car-

bon black was the best.

Electrochemical impedance spectroscopy (EIS, SolartronMultistat) measurements were carried out by applying an AC voltage of 5 mV in the frequency range of 100 kHz to 0.01 Hz. The active material served as the working electrode and lithium foil served as the counter and reference electrodes. The impedance response was measured before cycles.

3. Results and Discussion

Fig. 1 shows X-ray diffraction (XRD) pattern of WO_3 and WS_2 nanocrystals, WO-1, WO-2, WS-1, and WS-2, used in this study. The XRD peaks of WO-1 and WO-2 matched to all of the reference peaks of monoclinic phase WO_3 (JCPDS No. 43-1035; $P2_1/n$, a = 7.297 Å, b = 7.539 Å, c = 7.688 Å, b = 90.91º). The XRD pattern of WS-1, and WS-2 exhibits peaks corresponding to the hexagonal phase WS_2 (JCPDS No. 84-1398, $P6_3/mmc$, a = 3.153 Å and c = 12.323 Å). Therefore, all samples are pure without any other impurity phase.

Figs. 2a and 2b correspond to the scanning electron microscopy (SEM)/high-resolution transmission microscopy (HRTEM) images of WO-1 and WO-2, respectively. WO-1 exhibits the spherical shaped nanocrystal morphology with diameters in a wide range of 30-100 nm (average value = 50 nm). In contrast, WO-2 has the thin and long nanowire morphology with uniform diameter of 10 nm and the length of several micrometers. Lattice-resolved TEM and fast-Fourier-transform (FFT) images show that d-spacing of (020) planes is 3.8 Å, which is in good agreement with the reference value (3.7690 Å).

HRTEM images of WS-1 and WS-2 are shown in Figs. 2c and 2d, respectively. They both exhibit the nanosheet morphology, but the size is different: average size is 500 and 100 nm, respectively for WS-1 and WS-2. The thickness is estimated to be 50 and 10 nm, corresponding to 1/10 of the size. In the case of WS-2, the rolled edge of the nanosheets looks like nanowire, indicating that the nanosheets were grown from the lateral side of nanowires

Lattice-resolved TEM and FFT images at the zone axis of [001] reveal a highly crystalline basal plane. The d-spacing of {110} planes is 2.7 Å, which is in good agreement with the reference value (2.7307 Å). Fig. 2e show HRTEM and energy-dispersive X-ray spectroscopy (EDX) spectrum of WO-2, which iden-

tifies the W and O components using their M-shell and K-shell peaks. High-angle annular dark-field scanning TEM (HAADF STEM) image and EDX
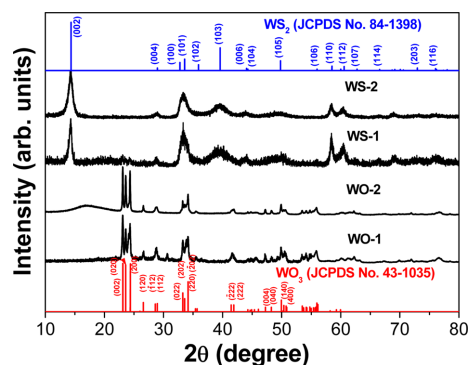

Fig. 1. XRD pattern of WO_3 (WO-1 and WO-2) and WS_2 (WS-1 and WS-2) nanocrystals. The peaks matched those of monoclinic phase WO_3 (JCPDS No. 72-1048) and hexagonal phase WS_2 (JCPDS No. 84-1398).
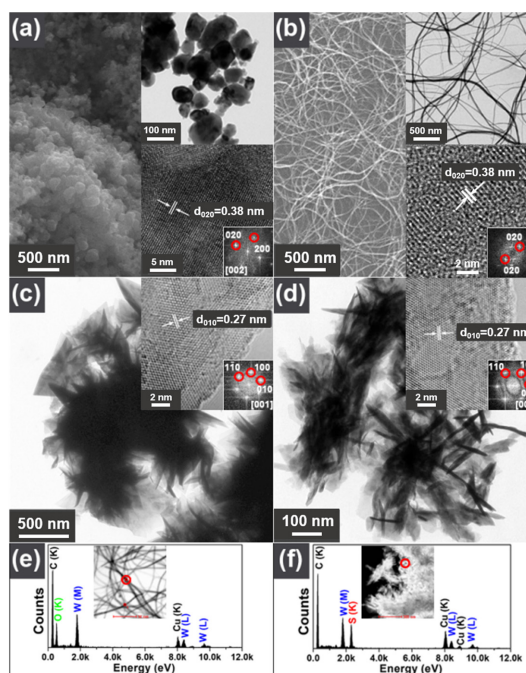

Fig. 2. SEM and TEM images showing the general morphology of (a) WO-1, (b) WO-2 (c) WS-1, and (d) WS-2. High-resolution TEM and corresponding FFT images reveal that the distance between the adjacent (010) planes (d_{020}) is 3.8 Å for monoclinic phase WO_3 nanocrystals and d_{010} is 2.7 Å for hexagonal phase WS_2 nanosheets. EDX spectrum shows the composition of (e) WO_3 (WO-2) and (f) WS_2 (WS-2).

spectrum are shown in Fig. 2f, proving that the nanosheets are composed of W and S with the atomic ratio of 1:2, using their M-shell and K-shell peaks. The Cu peak from the TEM Cu grid.

WO$_3$ reacts with H$_2$S to form WS$_2$, following the reaction represented by 2WO$_3$ + 4H$_2$S → 2WS$_2$ + 4H$_2$O + O$_2$. Since the diameter of WO$_3$ nanocrystal is similar to the thickness of WS$_2$ nanosheet, it is presumed that WO$_3$ nanocrystals adhere to form a sheet form during the sulfurization reaction of WO$_3$ at 400°C. The monoclinic phase WO$_3$ nanocrystals transformed to a thermodynamically stable hexagonal phase 2D structures of WS$_2$.

The LIB performance of WO$_3$ and WS$_2$ as active materials was examined using coin-type half-cells, as follows. The data are shown in Table 1 and Table 2. Before the description of the experimental data, let's examine the charge/discharge reaction of WO$_3$ and WS$_2$ in LIBs. The charge/discharge reaction of WO$_3$ and WS$_2$ is WO$_3$+ 6Li$^+$ + 6e$^-$ ↔ W + 3Li$_2$O and WS$_2$+ 4Li$^+$ + 4e$^-$W + 2Li$_2$S. respectively. In fact, the reversible reaction is 3O+ 6Li$^+$ + 6e$^-$ ↔ 3Li$_2$O and 2S+ 4Li$^+$ + 4e$^-$↔W + 2Li$_2$S. Since 1 mol of WO$_3$ and 6 mol of Li are reacting, the theoretical capacity of WS$_2$ is calculated as 6 ´ 26800 mA h mol^{-1} , 231.85 g mol^{-1} (molecular weight of WO$_3$) = 694 mA h g^{-1}. Since the 1 mol WS$_2$ react with 4 mol of Li, the theoretical

capacity of WS$_2$ is calculated as 4 × 26800 mA h mol^{-1} ÷ 247.99 g mol^{-1} (molecular weight of WS$_2$) = 694 mA h g^{-1}. 1C of WO$_3$ and of WS$_2$ was defined as 694 and 432 mA h g^{-1}. In addition, since we used a half-cell using Li metal as a negative electrode, the Li insertion is defined as discharging and the Li extraction as charging process.

Figs. 3a and 3b display the cyclic voltammetry (CV) curves of WO-1 and WO-2, respectively, for the first ten cycles. The CV curves were obtained by voltage scanning over the 0.01-3 V range at a rate of 0.1 mV s^{-1}. In the first cycle, the reduction peak appears at 0.4-0.6 V, due to a reaction in which WO$_3$ is reduced to produce W and Li$_2$O (WO$_3$+ 6Li$^+$ + 6e$^-$ → W + 3Li$_2$O), and a formation of solid electrolyte interface (SEI) layer at the surface of the electrode. The delithation reaction of Li$_2$O occurs at an oxidation peak of 1.0 V, and W is oxidized to become WO$_3$ at 2.0 V. After the first cycle, the reversible reaction occurs by insertion-extraction of Li ions at 0.8 V reduction peak and 1.1 V oxidation peak, respectively. The WO-2 exhibits a more pronounced oxidation-reduction peak.

Fig. 3c shows the 1, 5, 10, and 50 cycled charge/discharge curves of WO-1, and Fig. 3d displays the charge/discharge capacities vs. cycle number. The C-rate was 0.1 C (= 694 mA g^{-1}) and the charging and

Table 1. Summary of LIB half-cell capacities (mA h g^{-1}) of WO$_3$ and WS$_2$ nanocrystals during cycles at a rate of 0.1C.

Samples		First cycle			5th	50th	100th	
		discharge	charge	η (%)^a	discharge	discharge	discharge	η (%)^b
WO$_3$	WO-1	867	592	68.2	601	333	-	97.5
	WO-2	954	527	55.3	577	557	552	97.2
WS$_2$	WS-1	653	495	75.9	517	515	-	97.1
	WS-2	830	540	65.1	594	644	633	97.4

^{a} Coulombic Efficiency.
^{b} Coulombic Efficiency for 5~50 or 5~100 cycle

Table 2. Summary of the LIB half-cell capacities (mA h g^{-1}) of WO$_3$ and WS$_2$ nanocrystals as the rate is increased from 0.1 C to 5.0 C.

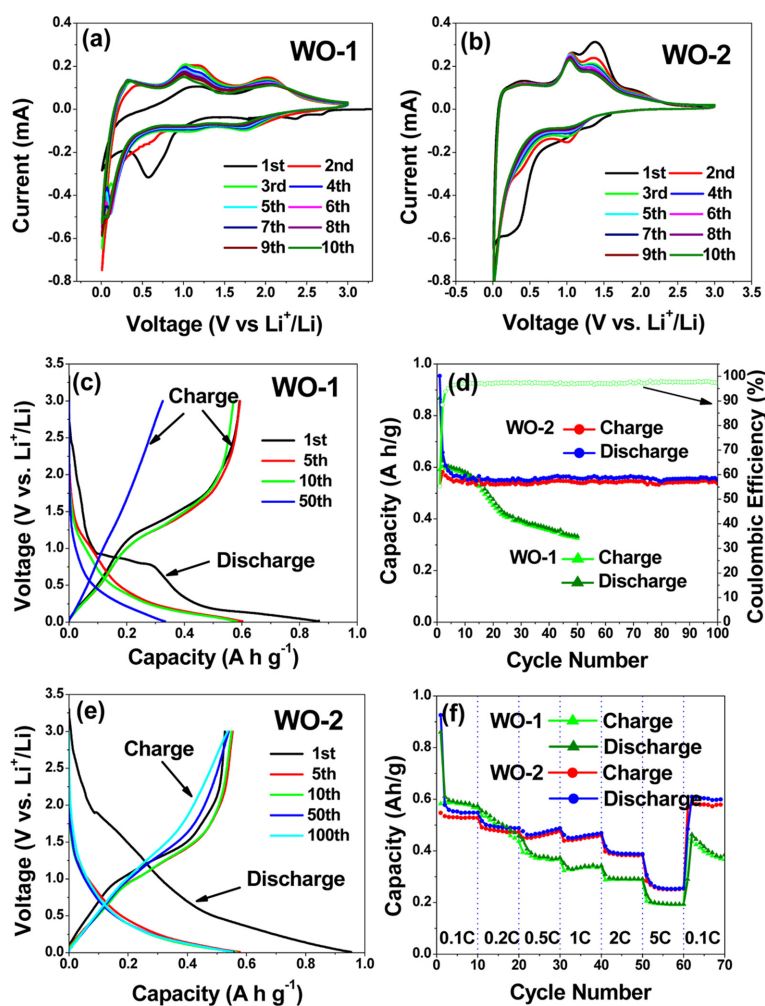| Samples		0.1 C	0.2 C	0.5 C	1 C	2 C	5 C	0.1 C
		5th	15th	25th	35th	45th	55th	65th
WO$_3$	WO-1	589	510	377	336	293	197	416
	WO-2	552	492	467	454	389	254	604
WS$_2$	WS-1	521	494	466	442	411	348	548
	WS-2	653	670	663	662	661	614	747

Fig. 3. Cyclic voltammetry curve of (a) WO-1 and (b) WO-2. (c) Charge and discharge voltage profiles of LIB half-cell using WO-1, tested between 0.01 and 3 V, at a rate of 0.1 C. (d) Charge/discharge capacity vs. cycle number for half cells using WO-1 and WO-2. The coulomb efficiency is plotted using the right axis. (e) Charge and discharge voltage profiles of LIB half-cell using WO-2, tested between 0.01 and 3 V, at a rate of 0.1 C. (f) Cycling performance of WO-1 and WO-2 as the C-rate is increased from 0.1 C to 5.0 C.

discharging CV curves were obtained by voltage scanning over the 0.01-3 V range at a rate of 0.1 C. The first discharge and charge capacities were 867 and 592 mA h g^{-1}, respectively, indicating a coulombic efficiency of about 68.2%. The large capacity loss in the first discharge step is interpreted to be due to the formation of SEI on the electrode surface. The flat region at 0.8 V and 1.1 V in the first discharge and charge curve is correlated with the reduction and oxidation peaks of the CV curve, respectively. As the cycle proceeds, the capacity decreases significantly.

In the 50th cycle, the discharge and charge capacities are 333 and 325 mA h g^{-1}, respectively, and the average coulombic efficiency of 2-50 cycles is 97.5%.

Fig. 3e shows the charge/discharge curves of WO-2 for 1, 5, 10, 50, and 100 cycles. Fig. 3d corresponds to the charge/discharge capacities vs. the number of cycles. The discharge and charge capacities of the first cycle were 954 and 527 mA h g^{-1}, respectively, indicating a coulombic efficiency of about 55.3%. Even though the cycle progresses, there is very little capacity reduction. In the 100th cycle, the discharge
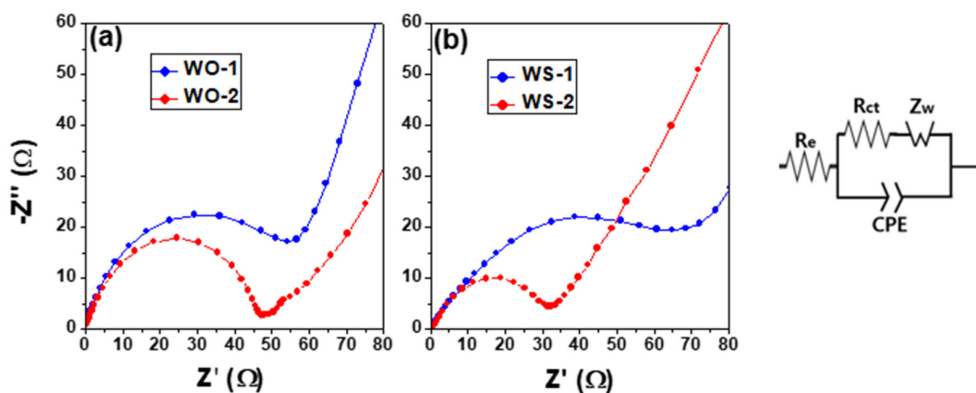
Fig. 4. Nyquist plots of (a) WO-1 and WO-2; (b) WS-1 and (b) WS-2, before the cycle of LIB. The equivalent circuit diagram is shown on the right.

and charge capacities were 552 and 537 mA h g^{-1}, respectively, and the average coulombic efficiency of 2-100 cycles was 97.2%, which is superior to WO-1, due to the more stable reversible reaction. The flat region of discharge curve at 1.0 V and that of charge curve at 1.1 V are in good coincidence with the reduction and oxidation peak of the CV curve.

Fig. 3f shows the charge/discharge capacity of step-wise 10 cycles by increasing the C-rate from 0.1 C to 0.2 C, 0.5 C, 1 C, 2 C, and 5 C, and the recovery capacities by lowering the C-rate to 0.1 C. The capacities in each step are summarized in Table 2. As the C-rate increased, the capacity decreased to 589, 510, 377, 336, 293, and 197 mA h g^{-1}. When it was reduced to 0.1 C, the capacity was 416 mA h g^{-1}, which was not recovered to the initial capacity at 0.1 C. On the other hand, WO-2 showed 552, 492, 467, 454, 389 and 254 mA h g^{-1} at 0.1 C, 0.2 C, 0.5 C, 1 C, 2 C, and 5 C, showing that the capacity is superior to that of WO-1. When the C-rate returns to 0.1 C, the initial capacity was recovered to 604 mA h g^{-1}. We conclude that WO-2 exhibits the higher capacity and the better reversibility under high-speed charge/discharge than WO-1.

Fig. 4a corresponds to Nyquist plots resulting from electrochemical impedance spectroscopy (EIS) before the cycle testing, consisted of one semicircle in the high-frequency region and a straight line in the low-frequency region. The equivalent-circuit (shown in right panel) curve-fit analysis was carried; R_e is the resistance of electrolyte, R_{ct} is the charge-transfer resistance between the active materials and the electrolyte, Z_W is the Warburg impedance corresponding

to the Li ion diffusion process, and CPE represents the constant-phase elements. The R_{ct} values of WO-1 and WO-2 are 70 W and 50 W, respectively, which is matched the larger capacity of WO-2 than that of WO-1. Therefore, as the surface area increases due to the reduction of size, the insertion/extraction of Li ions occurs more efficiently, and the charge transfer resistance between the electrode and the electrolyte decreases, which contribute in the capacity increase of the LIB. This result confirms that the size of the active material can greatly affect the capacity.

Figs. 5a and 5b show the CV data of WS-1 and WS-2, respectively, for the first ten cycles. The first cycle shows a broad cathodic peak in the 0.2-0.7 V region, which is due to lithiation ($WS_2 + xLi^+ + xe^- \rightarrow Li_xWS_2$) and the irreversible formation of SEI layers. After the first cycle, the reversible lithiation/delithiation signature of WS_2 ($WS_2 + xLi^+ + xe^- \leftrightarrow Li_xWS_2$) appeared consistently as a pair of lithiation (cathodic) cathodic and delithiation (anodic) peaks at potentials around 1.9 and 2.4 V, respectively, involving the reversible reaction. Once the SEI were formed during the 1st cycle, reversible reactions persisted over all subsequent cycles.

Fig. 5c shows charge-discharge curves for 1, 5, 10, and 50 cycles of WS-1. The C-rate was set to 0.1 C (43 mA g^{-1}) and the charge/discharge was performed between 0.01 V and 3 V. The discharge and charge capacities of the first cycle were greatly reduced from 653 to 495 mA h g^{-1}, respectively due to the formation of SEI and showed a coulombic efficiency of about 75.9%. The plateau of discharge and charge curves at 0.5 and 2.4 V, respectively, coincides with
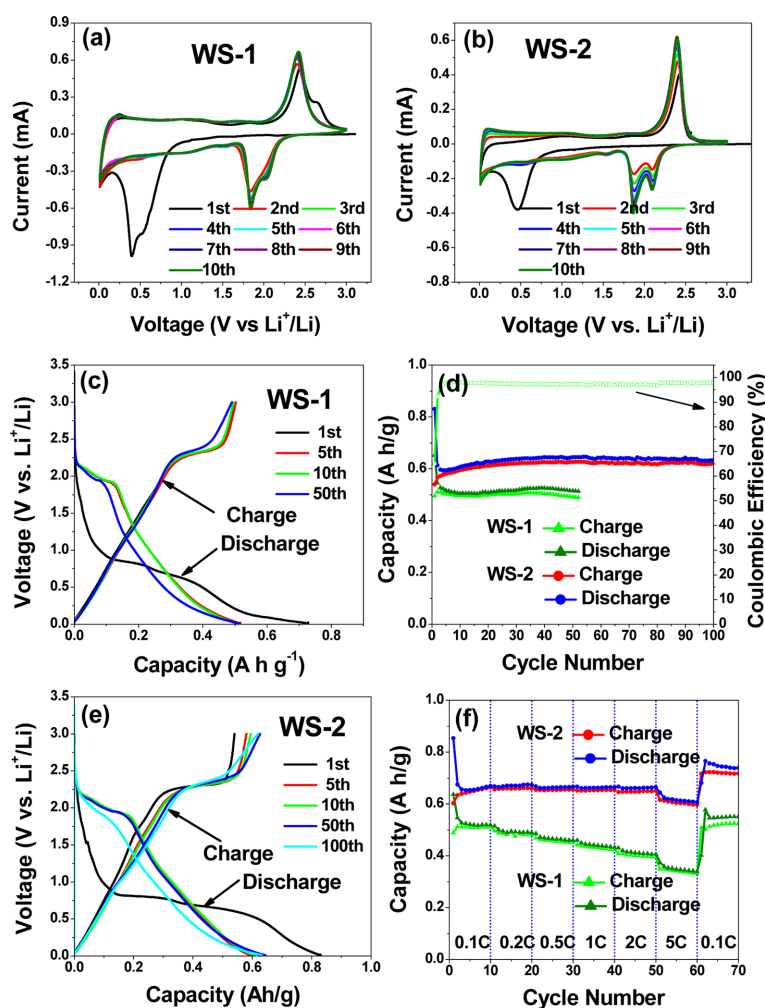
Fig. 5. Cyclic voltammetry curve of (a) WS-1 and (b) WS-2. Charge and discharge voltage profiles of LIB half-cell using (c) WS-1, tested between 0.01 and 3 V, at a rate of 0.1 C. (d) Charge/discharge capacity vs. cycle number for half cells using WS-1 and WS-2. The coulomb efficiency is plotted using the right axis. (e) Charge and discharge voltage profiles of LIB half-cell using WS-2, tested between 0.01 and 3 V, at a rate of 0.1 C. (f) Cycling performance of WS-1 and WS-2, as the C-rate is increased from 0.1 C to 5.0 C.

the reduction and oxidation peaks of the CV curve. Fig. 5d shows the charge/discharge capacity vs. the number of cycles. The capacity was stable and well maintained as 515 mA h g^{-1} after 50 cycles. The average coulombic efficiency is 97.1%. After the first cycle, the plateau of the discharge and charge curves at 1.9 V and 2.4 V, respectively, is in good coincidence with the reduction and oxidation peak of the CV curve.

Fig. 5e shows the charge/discharge curves of 1, 5, 10, 50 and 100 cycles of WS-2. Fig. 5d corresponds

to the charging and discharging capacities upon 100 cycling. The discharge and charge capacities of the first cycle were decreased from 830 to 540 mA h g^{-1}, respectively, and the coulomb efficiency was about 65.1%. For the first cycle, the plateau of discharge/charge curves at 0.5 and 2.4 V, respectively, corresponds to the reduction and oxidation peak of the CV curve. For 2-100 cycles, the plateau of discharge/charge curves at 1.9 and 2.4 V, respectively, corresponds to the reduction and oxidation peak of the CV curve. The capacity was maintained constant after

100 cycles and the capacity was 633 mA h g^{-1}. The average coulombic efficiency of 2-100 cycles is 97.4%, showing a better performance than WS-1.

Fig. 5f shows the cycling performance of WS-1 and WS-2 with the C rate changing in steps (0.1 C $\rightarrow$ 0.2 C $\rightarrow$ 0.5 C $\rightarrow$ 1 C $\rightarrow$ 2 C $\rightarrow$ 5 C $\rightarrow$ 0.1 C). The capacities in each step are summarized in Table 2. As the C-rate increased, the capacity of WS-1 decreased to 521, 494, 466, 442, 411, and 348 mA h g^{-1}. When it returned to 0.1 C, the capacity was recovered to more than 100% (548 mA h g^{-1}). WS-2 exhibited the larger charge/discharge capacity than WS-1; 653, 670, 663, 662, 661 and 614 mA h g^{-1}. When the C-rate return to 0.1 C, the capacity was sufficiently recovered to the initial value by 100% (747 mA h g^{-1}).

Fig. 4b shows the impedance data measured before the cycle of WS$_2$. The R_{ct} values o f WS-1 and WS-2 are 70 W and 30 W, respectively, indicating that WS-2 is smaller. This is consistent with the capacity of WS-2 being greater than WS-1. Therefore, as the size of the nanosheets decreases, the insertion and extraction of Li ions occurs more efficiently, and the charge transfer resistance between the electrode and the electrolyte decreases, which contribute in the capacity increase. This again confirms that the size of nanostructures can significantly affect the capacity of LIBs.

When comparing the capacities of WO$_3$ nanocrystals and WS$_2$ nanosheets, WO$_3$ nanocrystals (WO-2) show 552 mA h g^{-1}, which is slightly less than the theoretical capacity of 693 mA h g^{-1} after 100 cycles. The WS$_2$ nanosheet (WS-2), on the other hand, has 609 mA h g^{-1}, which is much higher than the theoretical capacity of 432 mA h g^{-1}. We conjecture that the capacity is increased because the reversible reaction distance is shortened because Li ions can enter or exit between the layers, which is an advantage of the 2D structure. The results of this study are compared with data published by other researchers (see Supporting Information, Table S1 and Table S2). Without the carbon complex, most capacity of WO$_3$ and WS$_2$ are below 500 mA h g^{-1}. As a follow-up study, we will try to increase the capacity by using carbon composites.

4. Conclusions

High purity WO$_3$ nanocrystals were synthesized by hydrothermal method and 2D WS$_2$ nanocrystals were synthesized from WO$_3$ nanocrystals by gas-phase sulfurization using H$_2$S gas at 400°C. The spherical-shaped WO$_3$ nanocrystals with an average diameter of 50 nm show 333 mA h g^{-1} after 50 cycles, whereas the uniformly thin WO$_3$ nanowires with 10 nm diameter exhibits a higher discharge capacity of 552 mA h g^{-1} after 100 cycles, which are slightly below the theoretical capacity of 693 mA h g^{-1}. Their Coulomb efficiencies are 97.5% for 50 cycles and 97.2% for 100 cycles, respectively. Thick WS$_2$ nanosheets synthesized using spherical WO$_3$ nanocrystals possess 300-500 nm in size, while thin WS$_2$ nanosheets synthesized using the WO$_3$ nanowires have a thickness of 10 nm and a size of 100 nm. The larger WS$_2$ nanosheets show 515 mA h g^{-1} after 50 cycles, but the smaller ones have a capacity of 633 mA h g^{-1} after 100 cycles and both nanosheets have a higher coulomb efficiency of over 97%. As the size decreases, lowering the charge transfer resistance between the electrode and the electrolyte are contributing to the capacity increase. In particular, WS$_2$ nanosheets have a much higher capacity than the theoretical capacity of 432 mA h g^{-1} by the advantages of 2D structures. The results of this study suggest that the morphology and size of nanocrystals can significantly affect the capacity, which contribute to the development of high-performance LIBs.

Acknowledgement

References

[1] JM.Tarascon and M. Armand, *Nature*, **2001**, *414*, 359-367.

[2] B. Dunn, H. Kamath and J. M. Tarascon, *Science*, **2011**, *334(6058)*, 928-935.

[3] V. Etacheri, R. Marom, R. Elazari, G. Salitra and D. Aurbach, *Energy Environ. Sci.*, **2011**, *4(9)*, 3243-3262.

[4] M. S. Whittingham, *Chem. Rev.* **2014**, *114(23)*, 11414-11443.

[5] X. Xu, W. Liu, Y. Kim, and J. Cho, *Nano Today*, **2014**, *9(5)*, 604-630.

[6] X. Hu, W. Zhang, X. Liu, Y. Mei and Y. Huang, *Chem. Soc. Rev.*, **2015**, *44(8)*, 2376-2404.

[7] S. H. Yu, S. H. Lee, D. J. Lee, Y. E. Sung and T. Hyeon, *Small*, **2016**, 12(*16*), 2146-2172.

[8] X. Cao, C. Tan, X. Zhang, W. Zhao and H. Zhang, *Adv. Mater.*, **2016**, *28(29)*, 6167-6196.

[9] L. Wang, S. Yue, Q. Zhang, Y. Zhang, Y. R. Li, C. S. Lewis, K. J. Takeuchi, A. C. Marschilok, E. S. Takeuchi and S. S. Wong, *ACS Energy Lett.*, **2017**, *2(6)*,1465-1478

[10] W. -J. Li and Z. -W. Fu, *Appl. Surf. Sci.*, **2010**, *256(8)*, 2447-2452.

[11] Y. Qiu, G. -L. Xu, Q. Kuang, S. -G. Sun and S. Yang, *Nano Res.*, **2012**, *5(11)*, 826-832.

[12] S. Yoon, S. -G. Woo, K. -N. Jung and H. Song, *J. Alloys. Comp.*, **2014**, *613*, 187-192.

[13] Y. Liu, Y. Jiao, H. Zhou, X. Yu, F. Qu and X. Wu, *Nano-Micro Lett.*, **2015**, *7(1)*, 12-16.

[14] Y. Sun, W. Wang, J. Qin, D. Zhao, B. Mao, Y. Xiao and M. Cao, *Electrochim. Acta*, **2016***, 187*, 329-339.

[15] H. Tong, Y. Xu, X. Cheng, X. Zhang, S. Gao, H. Zhao and L. Huo, *Electrochim. Acta*, **2016***, 210*, 147-154.

[16] X. Gu, F. Wu, B. Lei, J. Wang, Z. Chen, K. Xie, Y. Song, D. Sun, L. Sun, H. Zhou, and F. Fang, *J. Power Sources*, **2016***, 320*, 231-238.

[17] J. Xu, Y. Li, L. Wang, Q. Cai, Q. Li, B. Gao, X. Zhang, K. Huo and P. K. Chu, *Nanoscale*, **2016**, *8(37)*, 16761-16768.

[18] Z. Liu, P. Li, Y. Dong, Q. Wan, F. Zhai, A. A. Volinsky and X. Qu, *Appl. Surf. Sci.*, **2017***, 394*, 70-77.

[19] X. Wu and S. Yao, *Nano Energy*, **2017**, *42*, 143-150.

[20] K. Bao, W. Mao, G. Liu, L. Ye, H. Xie, S. Ji, D. Wang, C. Chen and Y. Li, *Nano Res.*, **2017**, *10(6)*, 1903-1911.

[21] G. X. Wang, S. Bewlay, J. Yao, H. K. Liu and S. X. Dou, *Electrochem. Solid-State Lett.*, **2004**, *7(10)*, A321-A323.

[22] K. Shiva, H. S. S. R. Matte, H. B. Rajendra, A. J. Bhattacharyya and C. N. R. Rao, *Nano Energy*, **2013**, *2(5)*, 787-793.

[23] D. Chen, G. Ji, B. Ding, Y. Ma, B. Qu, W. Chen and J. Y. Lee, *Nanoscale*, **2013**, *5(17)*, 7890-7896.

[24] X. Xu, C. S Rout, J. Yang, R. Cao, P. Oh, H. S. Shin and J. Cho, *J. Mater. Chem. A*, **2013**, *1(46)*, 14548-14554.

[25] Y. Liu, W. Wang, Y. Wang and X. Peng, *Nano Energy*, **2014**, *7*, 25-32.

[26] R. Chen, T. Zhao, W. Wu, F. Wu, L. Li, J. Qian, R. Xu, H. Wu, H. M. Albishri, A. S. Al-Bogami, D. A. El-Hady, J. Lu and K. Amine, *Nano Lett.*, **2014**, *14(10)*, 5899-5904.

[27] Z. Q. Duan, Y. C. Sun, Y. T. Liu, X. M. Xie and X. D. Zhu, *RSC Adv.*, **2014**, *4*, 41543-41550.

[28] W. Lv, J. Xiang, F. Wen, Z. Jia, R. Yang, B. Xu, D. Yu, J. He and Z. Liu, *Electrochim. Acta*, **2015**, *153*, 49-54.

[29] W. Yang, J. Wang, C. Si, Z. Peng, J. Frenzel, G. Eggeler and Z. Zhang, *J. Mater. Chem. A*, **2015**, *3(34)*, 17811-17819.

[30] Y. Du, X. Zhu, L. Si, Y. Li, X. Zhou and J. Bao, *J. Phys. Chem. C*, **2015**, *119(238)*, 15874-15881.

[31] H. Li, K. Yu, H. Fu, B. Guo, X. Lei and Z. Zhu, *Phys. Chem. Chem. Phys.*, **2015**, *17(44)*, 29824-29833.

[32] X. Zeng, Z. Ding, C. Ma, L. Wu, J. Liu, L. Chen, D. G. Ivey and W. Wei, *ACS Appl. Mater. Interfaces*, **2016**, *8(29)*, 18841-18848.

[33] Y. Wang, D. Kong, W. Shi, B. Liu, G. J. Sim, Q. Ge and H. Y. Yang, *Adv. Energy Mater.*, **2016**, *6(21)*, 1601057.

[34] L. Zhou, S. Yan, L. Pan, X. Wang, Y. Wang and Y. Shi, *Nano Res.*, **2016**, *9(3)*, 857-865.

[35] L. Zhang, W. Fan and T. Liu, *Nanoscale*, **2016**, *8(36)*, 16387-16394.

[36] S. Liu, B. Shen, Y. Niu and M. Xu, *J. Colloid. Interface Sci.*, **2017**, *488*, 20-25.